Proceedings of IMECE'02
2002 ASME International Mechanical Engineering Congress and Exposition
New Orleans, Louisiana, November 17-22, 2002

IMECE2002/NCA-32737

ADAPTIVE TIME-DISCONTINUOUS GALERKIN METHODS FOR ACOUSTIC SCATTERING IN UNBOUNDED DOMAINS

Lonny L. Thompson and Dantong He
Clemson University, Department of Mechanical Engineering
Clemson, South Carolina 29634-0921 USA
email: lonny.thompson@ces.clemson.edu

ABSTRACT

Comprehensive adaptive procedures with efficient sparse multi-level iterative solution algorithms for the time-discontinuous Galerkin space-time finite element method (DGFEM) including high-order accurate nonreflecting boundary conditions (NRBC) for unbounded wave problems are developed. The strategy requires only a few iterations per time step to resolve the solution to high accuracy. Further cost savings are obtained by decoupling the mass and boundary damping matrices in the algebraic structure giving rise to an explicit iterative method. An h-adaptive space-time strategy is employed based on a superconvergent patch recovery (SPR) technique, together with a temporal error estimate arising from the discontinuous jump between time steps in the DGFEM. For accurate data transfer (projection) between meshes, new superconvergent interpolation (SI) procedures are developed. Numerical studies of transient acoustic scattering demonstrate the accuracy, reliability and efficiency gained from the adaptive strategy.

INTRODUCTION

The accurate numerical simulation of waves governed by hyberbolic equations is important in many fields of physics, including computational hydro-acoustics, bio-acoustics, and aero-acoustics. To model wave propagation governed by the second-order wave equation in unbounded domains, often an artificial truncation boundary is introduced. Various treatments have been proposed to model the exterior field on this boundary. Promising methods include accurate nonreflecting radiation conditions, infinite elements, and absorbing layers.

The resulting bounded interior problem is often discretized with finite elements, resulting in a second-order system of ordinary differential equations in time, which are then solved with a finite difference time-stepping scheme such as the explicit central difference method or the implicit Newmark family and related methods. For modeling wave propagation, the conventional approach is to use explicit methods which avoid matrix factorization to advance solutions at discrete time-steps. However, a difficulty with these methods is that they are only conditionally stable, requiring a small time step below a limit dictated by the size of the smallest elements in the mesh. As a result, they typically require a fixed quasi-uniform mesh. Because of this limitation, conditionally stable methods are not suitable for self-adaptive methods which require the freedom to automatically select time-step size and unstructured mesh distributions.

For adaptive methods, unconditionally stable time-stepping methods are needed. A standard approach is to apply second-order implicit methods commonly used for structural dynamics applications, such as trapezoidal and select Newmark and related methods. However, for problems involving the propagation of pulses with broad band frequency content over large distances, commonly used second-order accurate numerical algorithms may exhibit significant dispersion errors causing misrepresentation of arrival time and directionality at a distant target. High-order accurate methods reduce these problems significantly.

One of the most promising high-order time-stepping methods are the time-discontinuous Galerkin space-time finite element methods (DGFEM) which employ finite element discretization of the time domain as well as the usual discretization of the spatial domain, [1-10]. The DGFEM possesses high-order accuracy and is unconditionally stable [1]. The principal features of the proposed DGFEM are: (i) higher-order polynomial approximations with self-adaptive unstructured meshes in both space and time dimensions, (ii) exponential rates of convergence can be achieved in space and time, (iii) algebraic form provides natural setting for predictor/corrector and iterative solvers for high-performance parallel computation.

Collectively, these features give promise of significant advances in efficiency, reliability, and flexibility in simulation software designed for transient acoustic waves. High-order space-time finite element methods are capable of delivering very high accuracies for wave propagation simulations over large distance and time, particularly for problems involving sharp gradients in the solution which typically arise in the vicinity of fluid-structure interfaces and near inhomogeneities such as stiffeners, structural joints, and material discontinuities. In these problems, solutions obtained with standard second-order time-integration methods may have difficulty resolving the discontinuities in the physical solution – large spurious oscillations may appear which pollute the entire solution.

In this work, comprehensive adaptive procedures using the DGFEM including the high-order accurate nonreflecting boundary conditions given in [11-16], for unbounded wave problems are developed. In particular, a multi-field DGFEM is formulated for the coupled interior/boundary equation problem with independent displacement and velocity variables for the interior wave equation together with auxiliary functions appearing in the nonreflecting boundary conditions. For problems of acoustics, the independent field variables in the multi-field formulation are pressure and velocity potential fields, [8].

To obtain efficient solutions, matrix structures are derived for the time-discontinuous Galerkin finite element methods (DGFEM) for hyperbolic equations. A sparse multi-level iterative scheme based on the Gauss-Seidel method is developed to solve the resulting fully-discrete system equations for the interior hyperbolic equations coupled with the first-order temporal equations associated with the nonreflecting boundary conditions. Due to the local nature of wave propagation, the strategy requires only a few iterations per time step to resolve the solution to high accuracy. In this work, the methods are implemented in two-dimensions, however, the procedures are also valid in three-dimensions.

The goal of an adaptive solution is to control space and time approximation error with minimal cost. The tools which enable the adaptive process are: 1. Error estimation, 2. Adaptation of the spatial mesh and/or time step size, and 3. Data transfer (projection) of solutions from a previous mesh to a current mesh. In this paper we use an adaptive strategy similar to Li and Wiberg [9,10]. An h-adaptive space-time strategy is employed based on the Zienkiewicz-Zhu [17,18] spatial error estimate using a superconvergent patch recovery (SPR) technique, together with a temporal error estimate arising from the discontinuous jump in solutions between time steps. As wave pulses propagate throughout the mesh, elements are refined near wave fronts, and unrefined where the solution is smooth or quiescent, providing efficient wave tracking over large distance and time. Errors in the time integration of both the interior equations and auxiliary functions in the nonreflecting boundary conditions are monitored with time-step adjustments to maintain given error tolerances.

Adaptive space-time finite element methods require projection of solutions from the previous space-time mesh to the current space-time mesh. For low-order elements, standard nodal interpolation may lead to significant accumulation of error over time. To correct this difficulty, we develop a new superconvergent interpolation (SI) method for the low-order 3-node triangle. The solution from the previous time-step is post-processed with the SPR technique with recovered gradients evaluated at midpoints between a node in the current mesh and interpolated between nodes in an element of the previous mesh. The result is a correction to standard interpolation with improved accuracy. The SI procedures are easily extended to tetrahedra.

WAVE EQUATION ON UNBOUNDED DOMAINS

We consider time-dependent acoustic waves in an infinite two-dimensional region $\mathcal{R}$, surrounding an object with surface $\mathcal{S}$. For computation, the unbounded region $\mathcal{R}$ is truncated by an artificial circular boundary Γ, of radius R. We then denote by $\Omega \subset \mathcal{R}$, the finite subdomain bounded by $\partial\Omega = \Gamma \cup \mathcal{S}$, see Fig. 1. Within Ω, the solution $u(\boldsymbol{x}, t)$, satisfies the scalar wave equation,

$$\frac{1}{c^2}\dot{v} \;=\; \nabla^2 u \;+\; f(\boldsymbol{x}, t), \qquad v = \dot{u}, \tag{1}$$

with initial conditions, $u(\boldsymbol{x}, 0) = u_0(\boldsymbol{x}), v(\boldsymbol{x}, 0) = v_0(\boldsymbol{x})$. Here and elsewhere a superimposed dot indicates differentiation with respect to time. We assume the wave speed is real valued with $c > 0$. For acoustics, u may be considered the pressure fluctuation from a reference state. Assuming linear irrotational fluids, u may also represent a velocity potential field. To specify radiation or scattering directly on

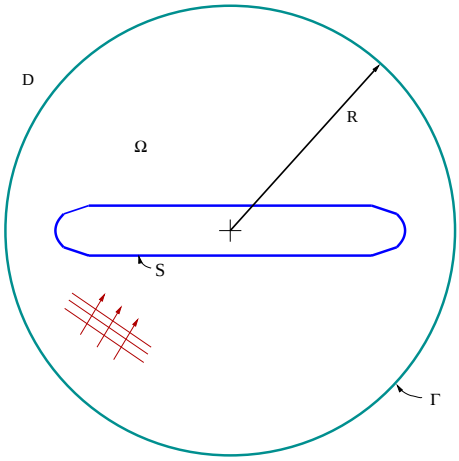

Figure 1. Illustration of two-dimensional unbounded region surrounding a scatterer $\mathcal{S}$.

the surface $\mathcal{S}$, we can specify a Neumann boundary condition,

$$\frac{\partial u}{\partial n} = g(\boldsymbol{x}, t), \qquad \boldsymbol{x} \in \mathcal{S}. \tag{2}$$

In linear acoustics, the condition $g = 0$, corresponds to a 'rigid' scatterer. The solution evaluated on the circular truncation boundary at $r = R$, is denoted by,

$$u_\Gamma(\theta, t) = u(R, \theta, t), \qquad v_\Gamma(\theta, t) = \dot{u}_\Gamma. \tag{3}$$

Let $\boldsymbol{w}(\theta, t) = \{w_j(\theta, t)\}_{j=1}^J$, be defined as a time-dependent vector of J, real valued scalar auxiliary functions, $\boldsymbol{w} = (w_1\,, w_2\,, \cdots, w_J)$. We expand the auxiliary functions $\boldsymbol{w}(\theta, t)$ and solution on the truncation boundary $u_\Gamma(\theta, t)$ by a Fourier series with M modes,

$$u_\Gamma(\theta, t) = \sum_{m=-M}^{M} u_m(t)\ \mathrm{e}^{im\theta}, \tag{4}$$

$$\boldsymbol{w}(\theta, t) = \sum_{m=-M}^{M} \boldsymbol{w}_m(t)\ \mathrm{e}^{im\theta} \tag{5}$$

In the above, $u_m(t)$, and $\boldsymbol{w}_m(t) = \{w_{m,j}\}_{j=1}^J$, are complex-valued modes defined by the tangential Fourier transform:

$$u_m(t) = \frac{1}{2\pi} \int_0^{2\pi} u_\Gamma(\theta, t)\ \mathrm{e}^{-im\theta}\, d\theta, \tag{6}$$

$$\boldsymbol{w}_m(t) = \frac{1}{2\pi} \int_0^{2\pi} \boldsymbol{w}(\theta, t)\ \mathrm{e}^{-im\theta}\, d\theta. \tag{7}$$

Here $u_m = u^*_{-m}$, and $\boldsymbol{w}_m = \boldsymbol{w}^*_{-m}$, with the asterisk denoting the complex conjugate, and $i = \sqrt{-1}$. The use of complex valued functions is used for conciseness of presentation; in practice the Fourier series is coded with real valued even $\cos m\theta$, and odd $\sin m\theta$, functions.

Using this expansion we then approximate the exterior impedance on Γ, by the high-order accurate radiation boundary conditions derived in [12]:

$$\left.\frac{\partial u}{\partial r}\right|_{r=R} + \frac{1}{c} v_\Gamma(\theta, t) + \frac{1}{2R} u_\Gamma(\theta, t) = \frac{1}{R} \sum_{m=-M}^{M} w_{m,1}(t)\, \mathrm{e}^{im\theta} \tag{8}$$

$$\dot{\boldsymbol{w}}_m(t) + \boldsymbol{A}_m\, \boldsymbol{w}_m(t) = \boldsymbol{b}_m\, u_m(t), \quad m \in (-M, M) \tag{9}$$

with initial condition $\boldsymbol{w}_m(0) = 0$. In the above, $\boldsymbol{w}_m(t)$ are time-dependent vector functions of order J, and $\boldsymbol{A}_m = \{A_m^{ij}\}_{i,j=1}^J$, is a tri-diagonal matrix for each mode m, defined with band:

$$\boldsymbol{A}_m = \frac{c}{4R} \left[m^2 - (j - 1/2)^2\,,\ 4j\,,\ -4\right] \tag{10}$$

The constant vector $\boldsymbol{b}_m = \{b_{m,j}\}_{j=1}^J$ is defined by $\boldsymbol{b}_m = \frac{c}{8R}(1 - 4m^2)\, \boldsymbol{e}_1$, $\boldsymbol{e}_1 = \{\delta_{j1}\}_{j=1}^J$.

The system (9) is a set of coupled first-order ordinary differential equations for each vector $\boldsymbol{w}_m(t)$, with dimension J, and driven by the boundary modes $u_m(t)$. We denote the sequence of boundary conditions by RBC(M, J), where M defines the number of modes included in the Fourier series, and J defines the boundary condition order. Typically, $J \ll M$, with the number of modes M dictated by the number of terms needed to resolve the solution $u_\Gamma(\theta, t)$ with a Fourier series on the circular truncation boundary. In [12], it has been shown that the boundary equations are well-posed and stable. The right-hand-side of (8) may be considered a correction to the approximate local B_1 operator of Bayliss and Turkel [20]. As more functions J, are included, the function w_1 on the RHS of (8) approaches an asymptotically exact correction to the approximate B_1 boundary condition.

TIME-DISCONTINUOUS GALERKIN FORMULATION

The development of the space-time method proceeds by considering a partition of the total time interval, $t \in (0, T)$, of the form: $0 = t_0 < t_1 < \cdots < t_N = T$, into N time intervals $I_n = \{(t_n, t_{n+1})\}_{n=0}^{N-1}$. The length of the variable time step is given by $\Delta t_n = t_{n+1} - t_n$. Using this notation, $Q_n = \Omega \times I_n$, are the nth space-time slabs.

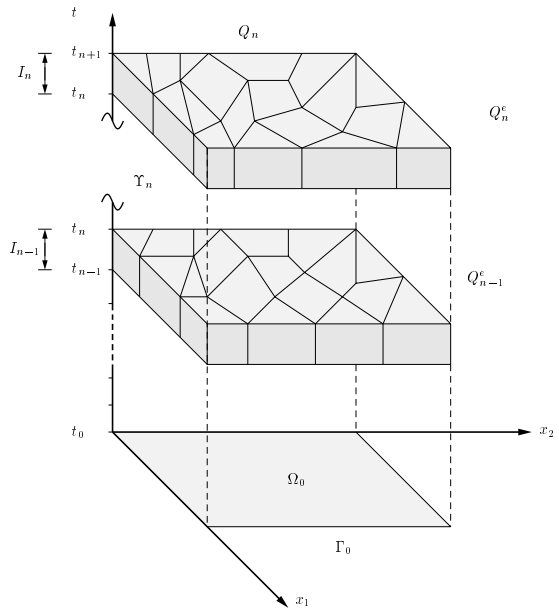

Figure 2. Illustration of two consecutive space-time slabs with different meshes.

Fig. 2 shows an illustration of two consecutive space-time slabs Q_{n-1} and Q_n, each with different meshes. Within each space-time element, the trial solution and weighting function are approximated by a finite basis which depend on both spatial $\boldsymbol{x}$, and temporal t, dimensions. The basis functions are assumed $C^0(Q_n)$ continuous throughout each space-time slab, but are allowed to be discontinuous across the interfaces of the slabs. The space of finite element basis functions in a multi-field representation is stated in terms of *independent* variables u, and v.

An important component in the stability and robustness of the space-time method is the incorporation of discontinuous temporal jump terms at each space-time slab interface. We define the one-sided limits of a piecewise continuous function u, as, for $s > 0$:

$$u(\boldsymbol{x}\,,\, t_n^+) = \lim_{s\to 0} u(\boldsymbol{x}, t_n + s),$$
$$u(\boldsymbol{x}\,,\, t_n^-) = \lim_{s\to 0} u(\boldsymbol{x}, t_n - s)$$

and set the jump operator across space-time slabs as the difference in the discontinuous solution,

$$[\![u(t_n)]\!] \,=\, u(\boldsymbol{x}\,,\, t_n^+) \,-\, u(\boldsymbol{x}\,,\, t_n^-).$$

In the following we define standard L_2 inner products by, $(w\,,\, u) = \int_\Omega w\, u\, d\boldsymbol{x}$ equipped with norm $||u||_\Omega = (u\,,\, u)^{1/2}$. Integrals on boundaries are defined by, $(w\,,\, u)_\Gamma = \int_\Gamma w\, u\, d\Gamma$, $(w\,,\, u)_S = \int_S w\, u\, dS$. For the circular radiation boundary Γ, we define the norm,

$$||u||_\Gamma^2 := \frac{1}{2R}(u,u)_\Gamma = \frac{1}{2R}\int_0^{2\pi} u_\Gamma^2(\theta,t)\, R\, d\theta \tag{11}$$

From Parseval's equality, $\lim_{M\to\infty} ||u_M||_\Gamma^2 = ||u||_\Gamma^2$,

$$||u_M||_\Gamma^2 = \pi \sum_{m=-M}^{M} u_m^2(t) \tag{12}$$

Define the real and imaginary part as, $u_m^c = 2\,\mathrm{Re}(u_m)$, $u_m^s = -2\,\mathrm{Im}(u_m)$, then,

$$||u_M||_\Gamma^2 = \frac{\pi}{2}\left\{\frac{1}{2}(u_0^c)^2 + \sum_{m=1}^{M}[(u_m^c)^2 + (u_m^s)^2]\right\}$$

The problem statement using the time-discontinuous Galerkin method (DGFEM) may be stated as,
Given: Load data $f\,,\, g$, and initial conditions $\{u(\boldsymbol{x}, t_n^-), v(\boldsymbol{x}, t_n^-)\}$, $\boldsymbol{w}_m(t_n^-)$, from the previous time step, then for each space-time slab, $n = 0, 1, \ldots, N-1$;
Find: $\boldsymbol{u} = \{u(\boldsymbol{x},t), v(\boldsymbol{x},t)\}$, and $\boldsymbol{w}_m(t)$, $\boldsymbol{x} \in \Omega \cup \partial\Omega$, $t \in I_n = (t_n, t_{n+1})$, such that for all admissible functions $\bar{\boldsymbol{u}} = \{\bar{u}(\boldsymbol{x},t), \bar{v}(\boldsymbol{x},t)\}$, and $\bar{\boldsymbol{w}}_m(t)$, $m \in (-M, M)$, the following coupled integral equations are satisfied,

$$A(\bar{\boldsymbol{u}}\,,\, \boldsymbol{u})_n + B_\Gamma(\bar{\boldsymbol{u}}\,,\, \boldsymbol{u})_n = F_S(\bar{v})_n + 2\pi \sum_{m=-M}^{M} F_\Gamma(\bar{v}_m, w_{m,1})_n \tag{13}$$

$$A_\Gamma(\bar{\boldsymbol{w}}_m\,,\, \boldsymbol{w}_m)_n = b_{m,1}\, F_\Gamma(\bar{w}_{m,1}, u_m)_n, \quad m \in (-M, M) \tag{14}$$

with

$$
\begin{aligned}
A(\bar{\boldsymbol{u}}\,,\,\boldsymbol{u})_n \;:=\; & \int_{I_n} (\bar{v}\,,\,\frac{1}{c^2}\dot{v})\;\mathrm{d}t + \int_{I_n} (\nabla\bar{v}\,,\,\nabla u)\;\mathrm{d}t \\
& + \int_{I_n} (\nabla\bar{u}\,,\,\nabla\dot{u} - \nabla v)\;\mathrm{d}t \\
& + (\bar{v}(t_n^+)\,,\,\frac{1}{c^2}[\![v(t_n)]\!]) + (\nabla\bar{u}(t_n^+)\,,\,[\![\nabla u(t_n)]\!]) \\
B_\Gamma(\bar{\boldsymbol{u}}\,,\,\boldsymbol{u})_n \;:=\; & \int_{I_n} \frac{1}{c}(\bar{v}\,,\,v)_\Gamma\;\mathrm{d}t + \int_{I_n} \frac{1}{2R}(\bar{v}\,,\,u)_\Gamma\;\mathrm{d}t \\
& + \int_{I_n} \frac{1}{2R}(\bar{u}\,,\,\frac{\partial u}{\partial t} - v)_\Gamma\;\mathrm{d}t \\
& + \frac{1}{2R}(\bar{u}(t_n^+)\,,\,[\![u(t_n)]\!])_\Gamma
\end{aligned}
$$

$$
\begin{aligned}
A_\Gamma(\bar{\boldsymbol{w}}_m\,,\,\boldsymbol{w}_m)_n \;:=\; & \int_{I_n} \bar{\boldsymbol{w}}_m(t)\cdot\dot{\boldsymbol{w}}_m(t)\;\mathrm{d}t \\
& + \int_{I_n} \bar{\boldsymbol{w}}_m(t)\cdot\boldsymbol{A}_m\,\boldsymbol{w}_m(t)\;\mathrm{d}t \\
& + \bar{\boldsymbol{w}}_m(t_n^+)\cdot[\![\boldsymbol{w}_m(t_n)]\!] \\
F_S(\bar{v})_n \;:=\; & \int_{I_n} \{(\bar{v}\,,\,f) + (\bar{v}\,,\,g)_S\}\;\mathrm{d}t \\
F_\Gamma(\bar{v}_m, w_{m,1})_n \;:=\; & \int_{I_n} \bar{v}_m(t)\,w_{m,1}(t)\;\mathrm{d}t, \\
F_\Gamma(\bar{w}_{m,1}, u_m)_n \;:=\; & \int_{I_n} \bar{w}_{m,1}(t)\,u_m(t)\;\mathrm{d}t, \\
\bar{v}_m(t) \;=\; & \frac{1}{2\pi R}(\bar{v}\,,\,\mathrm{e}^{im\theta})_\Gamma \\
u_m(t) \;=\; & \frac{1}{2\pi R}(u\,,\,\mathrm{e}^{-im\theta})_\Gamma
\end{aligned}
$$

The solution is obtained by solving the coupled variational problem (13)-(14), for a time interval $I_n = (t_n, t_{n+1}) = (t_1, t_2)$, with length $\Delta t_n = t_2 - t_1 > 0$. The source $f(\boldsymbol{x}, t)$, Neumann data $g(\boldsymbol{x}, t)$, initial conditions from the previous time-step $\{u(\boldsymbol{x}, t_n^-), v(\boldsymbol{x}, t_n^-)\}$, and $\boldsymbol{w}_m(t_n^-)$, are the known data on the current time slab. Coupling occurs through drivers $\boldsymbol{w}_m(t)$ on the right-hand-side of Eq. (13), and boundary modes $u_m(t)$, defined by (6) on the right-hand-side of (14). The far-field solution in the exterior region $\mathcal{D} = \mathcal{R} - \Omega$. may be computed concurrently with the solution in Ω using the methods described in [12,14].

The jump terms across space-time slabs are crucial for establishing an unconditionally stable algorithm for adaptive and unstructured space-time finite element discretizations, [1-3,16].

SPACE-TIME DISCRETIZATION

In this work, we assume we assume an orthogonal space-time discretization, within the space-time slabs, $Q_n = \Omega \times I_n$,

$$
u(\boldsymbol{x}, t) = \sum_{i=1}^{2} u_i^h(\boldsymbol{x})\phi_i(t) = \boldsymbol{N}_n(\boldsymbol{x}) \sum_{i=1}^{2} \phi_i(t)\boldsymbol{d}_i \tag{15}
$$

The temporal approximation is assumed linear with basis functions $\{\phi_i\}_{i=1}^2 \in \mathcal{P}^1(I_n)$. In general, the basis functions may be high-order spectral, defined by continuous Lagrange interpolation, or hp-version, defined by hierarchical Legendre polynomials. The FE approximations $\{u_i^h(\boldsymbol{x})\}$ are defined by a linear combination of spatial basis functions $N_A(\boldsymbol{x})$, and nodal values $\boldsymbol{d}_i = \{u_A(t_i)\}_{A=1}^D$, where D is the number of spatial nodes. The solution at the beginning of a time-interval is denoted, $t_1 = t_n^+$, and end, $t_2 = t_{n+1}^-$, the initial condition from the previous step is denoted $t_0 = t_n^- = t_{n-1}^+$. Similarly,

$$
v(\boldsymbol{x}, t) = \sum_{i=1}^{2} v_i^h(\boldsymbol{x})\phi_i(t) = \boldsymbol{N}_n(\boldsymbol{x}) \sum_{i=1}^{2} \phi_i(t)\boldsymbol{v}_i. \tag{16}
$$

Finally, the time-dependent auxiliary functions are approximated by,

$$
\boldsymbol{w}_m(t) = \sum_{i=1}^{2} \phi_i(t)\,\boldsymbol{w}_m(t_i) \tag{17}
$$

MATRIX EQUATIONS

Substituting the space-time approximations (15)-(17) into the variational equation (13) and integrating over a time interval (t_1, t_2), leads to the fully discrete matrix problem,

$$
\begin{bmatrix} \hat{\boldsymbol{M}} & \hat{\boldsymbol{M}}_{12} \\ \hat{\boldsymbol{M}}_{21} & \hat{\boldsymbol{M}} \end{bmatrix} \begin{Bmatrix} \boldsymbol{v}_1 \\ \boldsymbol{v}_2 \end{Bmatrix} = \begin{Bmatrix} \hat{\boldsymbol{r}}_1 \\ \hat{\boldsymbol{r}}_2 \end{Bmatrix} \tag{18}
$$

$$\hat{\boldsymbol{M}} = \boldsymbol{M} + \frac{\Delta t}{4}\boldsymbol{C},$$
$$\hat{\boldsymbol{M}}_{12} = \frac{1}{6}\boldsymbol{M} - \frac{\Delta t}{12}\boldsymbol{C} - \frac{(\Delta t)^2}{12}\boldsymbol{K},$$
$$\hat{\boldsymbol{M}}_{21} = \frac{3}{2}\boldsymbol{M} + \frac{3\Delta t}{4}\boldsymbol{C} + \frac{(\Delta t)^2}{4}\boldsymbol{K},$$
$$\hat{\boldsymbol{r}}_1 = \frac{\Delta t}{12}(3\boldsymbol{f}_1 - \boldsymbol{f}_2 - 2\boldsymbol{K}\boldsymbol{d}_0) + \frac{1}{6}\boldsymbol{M}\boldsymbol{v}_0,$$
$$\hat{\boldsymbol{r}}_2 = \frac{\Delta t}{4}(3\boldsymbol{f}_1 + \boldsymbol{f}_2 - 4\boldsymbol{K}\boldsymbol{d}_0) + \frac{5}{2}\boldsymbol{M}\boldsymbol{v}_0,$$

In the above, the symmetric and sparse, mass, boundary damping, and stiffness matrices, are defined by,

$$\boldsymbol{M} = [M_{AB}], \quad M_{AB} = \frac{1}{c^2}(N_A, N_B) \tag{19}$$
$$\boldsymbol{C} = [C_{AB}], \quad C_{AB} = \frac{1}{c}(N_A, N_B)_\Gamma \tag{20}$$
$$\boldsymbol{K} = [K_{AB}], \quad K_{AB} = (\nabla N_A, \nabla N_B) + \frac{1}{2R}(N_A, N_B)_\Gamma \tag{21}$$

The contribution to the right-hand-side load vectors defined at the beginning $\boldsymbol{f}_1$, and end $\boldsymbol{f}_2$, of a time-step due to the coupling from the auxiliary function $w_{m,1}(t)$ are given by,

$$\boldsymbol{f}_j = 2\pi \sum_{m=-M}^{M} w_{m,1}(t_j)\boldsymbol{F}_m, \quad j = 1, 2$$

where, for each tangential mode,

$$\boldsymbol{F}_m = \{F_{m,A}\}, \quad F_{m,A} = \frac{1}{2\pi R}(N_A, e^{im\theta})_\Gamma$$

Once $\boldsymbol{v}_1$ and $\boldsymbol{v}_2$ are solved, then $\boldsymbol{d}_1$ and $\boldsymbol{d}_2$ may be computed by simple vector updates,

$$\boldsymbol{d}_1 = \boldsymbol{d}_0 + \frac{\Delta t}{6}(\boldsymbol{v}_1 - \boldsymbol{v}_2); \qquad \boldsymbol{d}_2 = \boldsymbol{d}_0 + \frac{\Delta t}{2}(\boldsymbol{v}_1 + \boldsymbol{v}_2).$$

A remarkable feature of this form is that for spectral interpolation in space, nodal quadrature may be used to diagonalize both $\boldsymbol{M}$ and $\boldsymbol{C}$, resulting in a complete decoupling of the equations of the upper and lower sub-block diagonals. In this case, each time step requires only matrix-vector products with $\hat{\boldsymbol{M}}_{12}$ at each iteration in the solution for $\boldsymbol{c}_1$ and $\boldsymbol{c}_2$. Wiberg and Li [9], derived a different form, with $\hat{\boldsymbol{M}} = \boldsymbol{M} + \frac{\Delta t}{2}\boldsymbol{C} + \frac{\Delta t}{6}\boldsymbol{K}$; this submatrix cannot be conveniently diagonalized because of the presence of $\boldsymbol{K}$.

The time discretization for the first-order boundary equations takes the form,

$$\begin{bmatrix} \boldsymbol{I} & -\hat{\boldsymbol{A}}_m^+ \\ \hat{\boldsymbol{A}}_m^- & \boldsymbol{I} \end{bmatrix} \begin{Bmatrix} \boldsymbol{w}_{m,1} \\ \boldsymbol{w}_{m,2} \end{Bmatrix} = \begin{Bmatrix} \hat{\boldsymbol{f}}_{m,1} \\ \hat{\boldsymbol{f}}_{m,2} \end{Bmatrix} \tag{22}$$

where

$$\hat{\boldsymbol{A}}_m^+ = \frac{1}{3}(\boldsymbol{I} + \Delta t\boldsymbol{A}_m); \qquad \hat{\boldsymbol{A}}_m^- = (3\boldsymbol{I} + \Delta t\boldsymbol{A}_m),$$
$$\hat{\boldsymbol{f}}_{m,1} = \frac{1}{3}(2\boldsymbol{w}_m(t_n^-) - \Delta t\, u_{m,2}\, \mathbf{b_m});$$
$$\hat{\boldsymbol{f}}_{m,2} = 4\boldsymbol{w}_m(t_n^-) + \Delta t\, u_{m,1}\, \mathbf{b_m}.$$

The solution for $\boldsymbol{w}_{m,1}$ and $\boldsymbol{w}_{m,2}$ is driven by $u_{m,j}$, the discrete Fourier transform of the interior field $u_\Gamma(\theta, t)$, via (6), evaluated on the radiation boundary Γ:

$$u_m(t) = \sum_{j=1}^{2} \phi_j(t)\, u_m(t_j), \quad u_m(t_j) = \boldsymbol{F}_m^* \cdot \boldsymbol{d}_j \tag{23}$$

In the above, the star indicates the complex conjugate of the vector $\boldsymbol{F}_m$. In practice, the complex form of $\boldsymbol{F}_m$ and $\boldsymbol{F}_m^*$ are implemented as real valued vectors. Efficient implementation schemes for the discrete Fourier transform are given in [12].

The order J used in the radiation boundary is typically $J < 10$, resulting in relatively small matrices $\boldsymbol{A}_m$. Since the system (22) is block diagonal, we use static condensation to write the Schur complement, and first solve,

$$\hat{\boldsymbol{A}}_{m,2}\, \boldsymbol{w}_{m,2} = \hat{\boldsymbol{f}}_{m,2} - \hat{\boldsymbol{A}}_m^-\, \hat{\boldsymbol{f}}_{m,1}, \tag{24}$$

with coefficient matrix,

$$\hat{\boldsymbol{A}}_{m,2} = (\boldsymbol{I} + \hat{\boldsymbol{A}}_m^- \hat{\boldsymbol{A}}_m^+)$$

then update, $\boldsymbol{w}_{m,1} = \hat{\boldsymbol{f}}_{m,1} + \hat{\boldsymbol{A}}_m^+ \boldsymbol{w}_{m,2}$.

The number of modes $m \in (-M, M)$ included depends on the complexity of the solution as measured by the amplitude of spatial angular wavelengths on the boundary Γ; typically $M \ll N_\Gamma$, where N_Γ is the number of nodes on the boundary. The primary cost in implementing the high-order radiation boundary conditions is not the solution of the relatively small equation system (22), or (24), but in the computation of the discrete Fourier transform $u_{m,j} = \boldsymbol{F}_m^* \cdot \boldsymbol{d}_j$. The vector $\boldsymbol{F}_m^*$ must be re-evaluated at each adaptive remeshing. Nevertheless, this cost is always less that that required to solve the interior equations (18); see [12] for complexity estimates and efficient methods for computing $\boldsymbol{F}_m^*$.

MULTI-LEVEL ITERATIVE SOLUTION ALGORITHM

For efficient equation solution, a multi-level iterative method is developed; system (18) is solved with a simple Gauss-Seidel iterative algorithm, while the relatively small system (22) is solved directly. Using the initial predictor from the previous time-step, only a few iterations are needed to solve the coupled equations within a small error tolerance. The algorithm is summarized in the following:

Denote the initial conditions by,
$\boldsymbol{d}_0 = \boldsymbol{d}(t_n^-)$, $\boldsymbol{v}_0 = \boldsymbol{v}(t_n^-)$, $\boldsymbol{v}_{-1} = \boldsymbol{v}(t_{n-1}^+)$.

1. Predict from previous step solution,

$$\boldsymbol{d}_1^0 = \boldsymbol{d}_0, \quad \boldsymbol{d}_2^0 = \boldsymbol{d}_0 + \boldsymbol{v}_0 \Delta t_n$$
$$\boldsymbol{v}_1^0 = \boldsymbol{v}_0, \quad \boldsymbol{v}_2^0 = \boldsymbol{v}_0 + \boldsymbol{a}_0 \Delta t_n, \quad \boldsymbol{a}_0 = (\boldsymbol{v}_0 - \boldsymbol{v}_{-1})/\Delta t_n$$

Two-Level Iterative Method:
Outer Iteration Loop: For $k = 0, 1, \ldots$
2. Compute boundary modes: $u_{m,i}^k = \boldsymbol{F}_m^* \cdot \boldsymbol{d}_i^k$.
3. Solve boundary equations (24):
4. Update: $\boldsymbol{w}_{m,1}^k = \hat{\boldsymbol{f}}_{m,1}^k + \hat{\boldsymbol{A}}_m^+ \boldsymbol{w}_{m,2}^k$.
Set: $\boldsymbol{v}_i^{(0)} = \boldsymbol{v}_i^k, \quad i = 1, 2.$
G-S Iteration Loop: For $l = 0, 1, \ldots$
5. Using the G-S method for the system:
$\hat{\boldsymbol{M}} \boldsymbol{v}_2 = \hat{\boldsymbol{r}}_2^k - \hat{\boldsymbol{M}}_{21} \boldsymbol{v}_1^{(l)}$, update $\boldsymbol{v}_2^{(l+1)}$.
6. Using the G-S method for the system:
$\hat{\boldsymbol{M}} \boldsymbol{v}_1 = \hat{\boldsymbol{r}}_1^k - \hat{\boldsymbol{M}}_{12} \boldsymbol{v}_2^{(l+1)}$, update $\boldsymbol{v}_1^{(l+1)}$.
If converged, Exit G-S Iteration Loop
End G-S Iteration Loop
Set: $\boldsymbol{v}_i^{k+1} = \boldsymbol{v}_i^{(l+1)}, \quad i = 1, 2.$
7. Update:
$\boldsymbol{d}_1^{k+1} = \boldsymbol{d}_0 + \frac{\Delta t}{6}(\boldsymbol{v}_1^{k+1} - \boldsymbol{v}_2^{k+1})$,
$\boldsymbol{d}_2^{k+1} = \boldsymbol{d}_0 + \frac{\Delta t}{2}(\boldsymbol{v}_1^{k+1} + \boldsymbol{v}_2^{k+1})$.
If converged, Exit Outer Iteration Loop.
End Outer Iteration Loop.

When performing the Gauss-Seidel (G-S) iterate in Steps 5 and 6, only the nonzero coefficients in the sparse matrices $\hat{\boldsymbol{M}}, \hat{\boldsymbol{M}}_{12}, \hat{\boldsymbol{M}}_{21}$ together with pointers to appropriate row/column numbers are stored in memory. When $\hat{\boldsymbol{M}} = \boldsymbol{M} + (\Delta t/4)\boldsymbol{C}$ is diagonalized using nodal quadrature the algorithm consists of simple scaling in Steps 5 and 6, with super fast solves. In this case the algorithm for the interior equations may be viewed as an *unconditionally stable explicit multi-corrector method*.

SUPERCONVERGENT INTERPOLATION

Projection of the solution from the previous to the current space-time slab is obtained by nodal interpolation. For low-order elements in space, standard nodal interpolation introduces significant error. To correct this difficulty, we have developed a new *superconvergent interpolation* scheme. Prior to projecting, the solution on the top of previous time-slab, $t_{n-1}^+ = t_n^-$, is interpolated with,

$$u(\boldsymbol{x}, t_n^-) = \sum_{A=1}^{D_{n-1}} N_A^-(\boldsymbol{x}) \left[u_A^h(t_n^-) + \hat{\boldsymbol{x}}_A \cdot \nabla u_A^*(\boldsymbol{x}_A^c, t_n^-) \right] \tag{25}$$

where, $\hat{\boldsymbol{x}}_A = \boldsymbol{x} - \boldsymbol{x}_A$, and the vector, $\nabla u_A^*(\boldsymbol{x}_A^c, t_n^-)$ is the recovered gradients obtained by superconvergent patch recovery (SPR) at node A, evaluated at the midpoint between node $\boldsymbol{x}_A$, and position $\boldsymbol{x}$. A similar technique is used for $v(\boldsymbol{x}, t_n^-)$. This scheme may be viewed as a correction to standard interpolation, and provides nearly an order-of-magnitude improvement in accuracy. It can be shown, that the extension to quadrilateral and tetrahedron elements is straightforward.

TEMPORAL ERROR INDICATOR

Define a norm composed of the total energy in the interior domain, Ω, plus an additional term consistent with the radiation boundary condition on Γ,

$$||\boldsymbol{u}||_n^2 = \frac{1}{c^2} \int_\Omega \left\{ v^2(t_n) + (\nabla u(t_n))^2 \right\} \, \mathrm{d}\boldsymbol{x} + \frac{1}{2R} \int_\Gamma u^2(t_n) \, \mathrm{d}\Gamma. \tag{26}$$

Consistent with the space-time variational equation (13), a natural measure of the temporal error at time t_n, is defined by the local temporal jump terms (residuals) across space-time slab interfaces,

$$||\boldsymbol{e}_t||_n^2 = \int_\Omega \left\{ \frac{1}{c^2} [\![v(t_n)]\!]^2 + [\![\nabla u(t_n)]\!]^2 \right\} \, \mathrm{d}\boldsymbol{x} + \frac{1}{2R} \int_\Gamma [\![u(t_n)]\!]^2 \, \mathrm{d}\Gamma \tag{27}$$

When solutions from the previous time-step are interpolated to the nodes of the current mesh, and for orthogonal space-time discretization of the form (15), then, (26) and (27) may be expressed in the quadratic matrix form,

$$||\boldsymbol{u}||_n^2 = \boldsymbol{d}_n(t_n) \cdot \boldsymbol{K}_n \boldsymbol{d}_n(t_n) + \boldsymbol{v}_n(t_n) \cdot \boldsymbol{M}_n \boldsymbol{v}_n(t_n) \tag{28}$$

$$||\boldsymbol{e}_t||_n^2 = [\![\boldsymbol{d}_n(t_n)]\!] \cdot \boldsymbol{K}_n [\![\boldsymbol{d}_n(t_n)]\!] + [\![\boldsymbol{v}_n(t_n)]\!] \cdot \boldsymbol{M} [\![\boldsymbol{v}_n(t_n)]\!] \tag{29}$$

where $\boldsymbol{K}_n$ and $\boldsymbol{M}_n$ are mass and stiffness matrices for the current step defined in (19),(21). A similar temporal error indicator was used for structural dynamics problems in

[9,10]. In that case, the boundary integral in (26) and (27), was neglected.

To maintain a specified level of accuracy at a given time step, the relative error is enforced to be below a specified tolerance:

$$\eta_t(t_n) = \frac{||\boldsymbol{e}_t||_n}{||\boldsymbol{u}||_n} \leq \eta_t^{TOL} \tag{30}$$

A new time step Δt_n^{new} is determined from the asymptotic temporal error estimate for the local error using a strategy similar to [10]. We introduce two real parameters $\beta_{t1} < 1.0$ and $\beta_{t2} > 1.0$ and one integer $K_t > 0$ to control the time step change. If $\eta_t > \eta_t^{TOL}$, then the solution is rejected and a *time-step refinement* is performed. If $\eta_t < \beta_{t1}\eta_t^{TOL}$, occurs K_t successive times, then the solution is accepted, and the time-step size is increased for the next time step. The parameter $\beta_{t2} > 1.0$ is used as a safety factor for accepting a new time-step size. For this purpose, we use a smaller value η_t^{TOL}/β_{t2} in place of the tolerance η_t^{TOL} in the formula in determining the new time step size. In this way, the error resulting from the new time-step will always satisfy $\eta_t < \eta_t^{TOL}$.

To control the temporal error in solving the radiation boundary functions, we define at each time step n, the L_2-norm on the boundary Γ,

$$||\boldsymbol{w}||_n^2 = \int_0^{2\pi} (\boldsymbol{w}(\theta, t_n^-))^2 \, d\theta = 2\pi \sum_{j=1}^{J} ||w_j||_n^2. \tag{31}$$

$$||w_j||_n^2 = \sum_{m=-M}^{M} (w_{m,j}(t_n^-))^2. \tag{32}$$

In the above, J is the number of auxiliary boundary functions used for each mode. Typically, $M = 20,\ J = 6$.

A local measure of the temporal error is then obtained by computing the residuals of the discontinuous solution at a time-step,

$$||\boldsymbol{e}_w||_n^2 = 2\pi \sum_{m=-M}^{M} (\llbracket \boldsymbol{w}_m(t_n) \rrbracket)^2 \tag{33}$$

We then monitor the relative error,

$$\eta_w = \frac{||\boldsymbol{e}_w||_n}{||\boldsymbol{w}||_n} < \eta_w^{TOL}. \tag{34}$$

If the relative boundary error (34) exceeds the tolerance η_w^{TOL}, the time step can be redefined similar to that used for the internal field variables u and v. In practice, the relative boundary error (34) is typically of the order of the error in the field variables, and the time step change for the coupled interior/boundary system is controlled by (30).

Typically, the acoustic field is initially localized to a compact region internal to the computational domain Ω. In this case, nonzero amplitudes for the field variables u and v will take time to reach the truncation boundary Γ, as dictated by the wave speed c. In this case, solutions to the boundary functions $\boldsymbol{w}_m$ can be 'turned-off', reducing to the local first-order B_1 condition. To identify the first occurrence of a nonzero amplitude, the boundary norm (12) is monitored, and the magnitude checked against a small tolerance. When the boundary norm exceeds this tolerance, then the boundary functions $\boldsymbol{w}_m$ are 'turned-on' in the coupled solution algorithms described earlier, with error monitored by (34).

SPATIAL ERROR ESTIMATION

For an estimate of the spatial error at a given time-step, we compute the difference between SPR and FEM gradients measured in the L_2 norm. The error is computed over each element Ω_e, and summed to give the global error,

$$||\boldsymbol{e}_s||_n^2 = \sum_{e=1}^{ne} ||\boldsymbol{e}_s||_{n,e}^2 \tag{35}$$

$$||\boldsymbol{e}_s||_{n,e}^2 = \int_{\Omega_e} [\nabla u^*(\boldsymbol{x}, t_{n+1}^-) - \nabla u^h(\boldsymbol{x}, t_{n+1}^-)]^2 \, \mathrm{d}\boldsymbol{x}$$

In the above, ∇u^* is the gradient obtained from the superconvergent patch recovery (SPR) technique [17], while ∇u^h, is the constant gradient approximation within each element. Since the recovered gradient ∇u^* converges at a higher rate than the FEM gradient ∇u^h, the effectivity of the error indicator, as measured by the ratio of the estimated error to the true error, is asymptotically exact, i.e., as the mesh is refined, the effectivity index will approach the optimal value of one, [18].

To control the spatial accuracy, the estimated relative error is kept below a specified tolerance:

$$\eta_s(t_n) = \frac{||\boldsymbol{e}_s||_n}{||u^h||_n} \leq \eta_s^{TOL} \tag{36}$$

Once the estimated error is calculated, and it is determined that a new mesh is required, an optimal mesh is obtained

by assuming equal distribution of error with the least number of required elements. The refinement condition which satisfies this optimal criteria is determined from,

$$h_e^{new} = h_e^{old}/\xi_e \tag{37}$$

where h_e^{old} denotes the characteristic size of element e, in the previous (old) mesh, and h_e^{new} is the desired size of the new elements in the region covered by that old element. The refinement parameter is defined on each element by [19]:

$$\xi_e = \frac{\eta_e^{1/(p+1)}}{(\eta_s^{TOL})^{1/p}} \left[\sum_{e=1}^{N_e} \eta_e^{2/(p+1)} \right]^{1/2p}, \qquad \eta_e = \frac{||\boldsymbol{e}_s||_{n,e}}{||u^h||_{n,e}} \tag{38}$$

In the above, p is the polynomial degree of the basis functions used in the mesh, and η_e is the contribution from element e to the estimated relative global error, η_s.

Similar to the adaptive strategy used to change time step size, we introduce two real parameters $\beta_{s1} < 1.0$ and $\beta_{s2} > 1.0$, and one integer $K_s > 0$. If $\eta_s > \eta_s^{TOL}$, then the solution is rejected and a *mesh refinement* is performed. If $\eta_s < \beta_{s1}\eta_s^{TOL}$, occurs K_s successive times, then the solution is accepted, and the mesh is redistributed to a coarser mesh. In order to satisfy $\eta_s < \eta_s^{TOL}$ with the new mesh, we use η_s^{TOL}/β_{s2} in place of the η_s^{TOL} in (38). To maintain geometric fidelity of boundary features, a maximum element size is enforced, $h_e < h_{max}$.

OVERVIEW OF ADAPTIVE STRATEGY

The overall adaptive solution process may be summarized in the following:

1. Generate initial mesh, and set initial time step size.
2. Loop over time steps,
   (a) Time Step Control within interval (t_n, t_{n+1}).
      i. Predict from previous step solution.
      ii. Solve coupled interior/boundary equations using multi-level iterative method.
      iii. Temporal error estimation.
      iv. If new time-step, update and return to 2(a).
   (b) Spatial error estimation.
   (c) If new mesh required, remesh and transfer (project) solution from previous mesh to new mesh, reform matrices and return to 2(a).
3. End Time Step Loop.

To manage cost, only one remesh is allowed per time-step.

1 SINUSOIDAL SCATTERING

To validate the accuracy of the DGFEM formulation with the multi-level iterative algorithm against a known solution, we first consider an incident plane-wave defined by a steady sinusoidal function for all time $t > \boldsymbol{\nu} \cdot (\boldsymbol{x} - \boldsymbol{x}_0)/c$:

$$u^{(i)}(\boldsymbol{x}, t) = -\sin[\omega(t - t_s)]\ H(t - t_s) \tag{39}$$

Here $H(t)$ is the unit-step (Heaviside) function.

We then consider the problem of scattering of an incident plane-wave traveling off-axis from an infinite elliptic cylinder. The ellipse is defined by coordinates $x = a\cos\theta$, and $y = b\sin\theta$, $(a, b) = f(\cosh\mu, \sinh\mu)$. Here we choose the radial coordinate $\mu_0 = 0.1$, with foci $f = 1$, such that $(a, b) = (1.005, 0.100)$, resulting in a 10:1 ratio. The cylinder is assumed rigid and infinite in the z-direction.

The direction of the incident plane-wave is determined by the unit wave vector $\boldsymbol{\nu} = [\cos\alpha, \sin\alpha]$, where $\alpha = 30^o$ is the angle between the lines of constant phase and the x-axis. The time delay, $t_s = \boldsymbol{\nu} \cdot (\boldsymbol{x} - \boldsymbol{x}_0)/c$, is proportional to the wave speed and position of the incident wave as it moves past the ellipse. Here $\boldsymbol{x}_0 = [x_0, y_0]$ defines the position of the initial wave front at $t = 0$.

For the space-time finite element solution, the radius of the circular radiation boundary Γ is set at $R = 1.25$, with RBC of order $J = 6$, and $M = 20$ circumferential modes. From previous studies, [12], the use of $J = 6$ is found to give accurate solutions for problems of this type. The initial mesh is shown in Fig. 3. The computation is driven from rest to steady-state with $c = 1$, and frequency $k = \omega/c = 2\pi$.

Fig. 7 shows the scattered field solution obtained by DGFEM. The corresponding adaptive mesh is shown in Fig. 8. The initial scattered field is localized to a compact region near the LHS of the ellipse. As the solution progresses the mesh is redistributed to efficiently track the transient wave front of the scattered field.

Fig. 9 shows the total energy norm for the scattered field within the computational domain. The energy starts from an initial zero state, and then increases as the incident wave progresses. After approximately $t = 2$, the transient solution reaches an initial steady-state. A full steady solution is reached after $t = 8$.

Fig. 5 shows the time-history at a representative observation point 1 on the bottom surface of the elliptic scatterer, see Fig. 4. The results show that the DGFEM solution with the high-order radiation boundary conditions are very accurate.

Fig. 6 shows the instantaneous L_2 error on Γ. By setting a smaller error tolerance in the adaptive solution, the error is reduced accordingly.

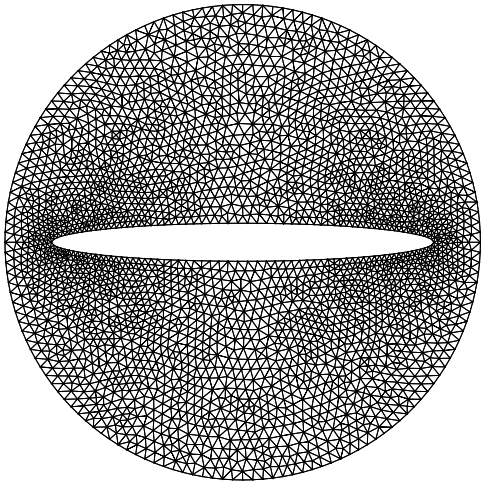

Figure 3. Computational domain defined by elliptic cylinder surrounded by circular radiation boundary. Initial mesh: 5700 elements, 2989 nodes.

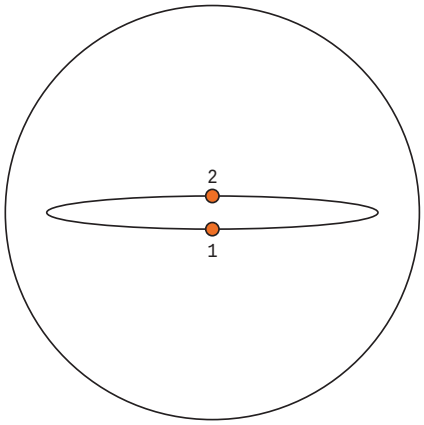

Figure 4. Illustration of observation points $(0, \pm b) = (0, -\sinh 0.1)$ on the bottom/top surface of the elliptic scatterer.

Fig. 10 and 11 shows the number of DOF and time-step size Δt_n during the adaptive solution process. The results show that in order to control the accuracy during the initial transient wave solution, the number of DOF in the mesh increases. At the same time, the time-step size is increased until the initial steady-state has been reached, near $t = 2$. After this time, both the spatial and temporal errors fall within the bounds set, and no remeshing or time-step changes are needed.

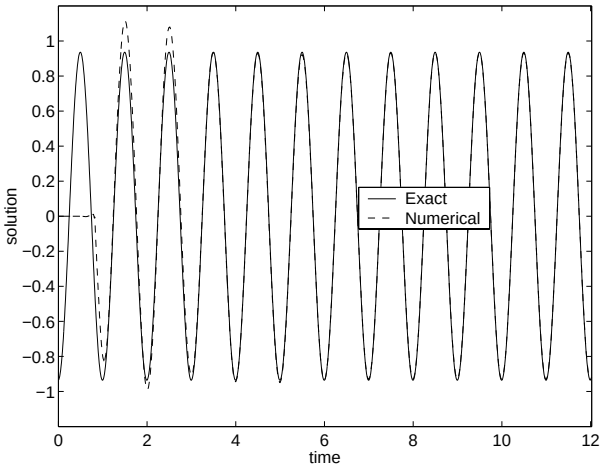

Figure 5. Solution at observation point 1.

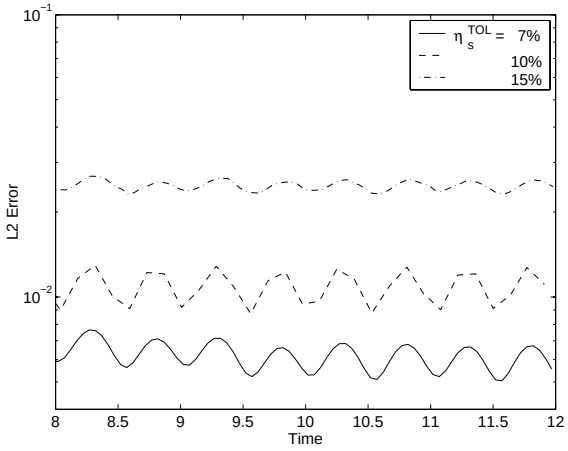

Figure 6. L2 error on radiation boundary, with $\eta_s^{TOL} = (15\%, 10\%, 7\%)$. Max L2 error = $(0.0268, 0.0130, 0.0076)$

RICKER PULSE SCATTERING

We next set the incident wave to be the finite duration wavelet,

$$u^{(i)}(\boldsymbol{x}, t) = g(t - t_s)\ h(\boldsymbol{x}, t), \tag{40}$$

defined by the modified Ricker pulse,

$$g(t) = \frac{(0.25\beta^2 - 0.5)e^{-0.25\beta^2} - 13e^{-13.5}}{0.5 + 13e^{-13.5}} \tag{41}$$

$$h(\boldsymbol{x}, t) = H(t - t_s) - H(t - t_s - 6\sqrt{6}/\omega_r)$$

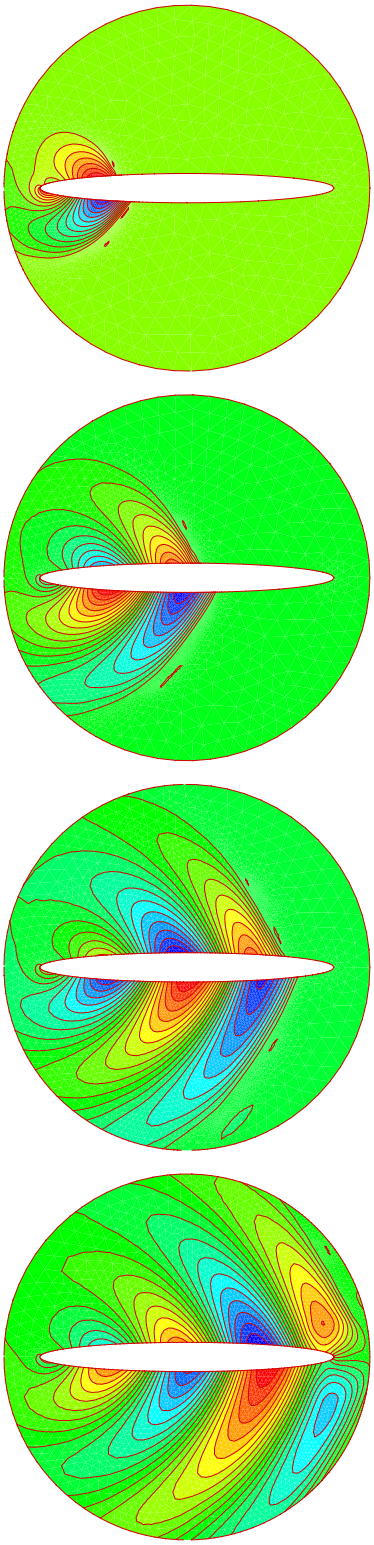

Figure 7. Scattered field DGFEM solution for sinusoidal incident plane wave at 30^o angle, at snapshots in time: t=0.5, 1.0, 1.5, 2.0.

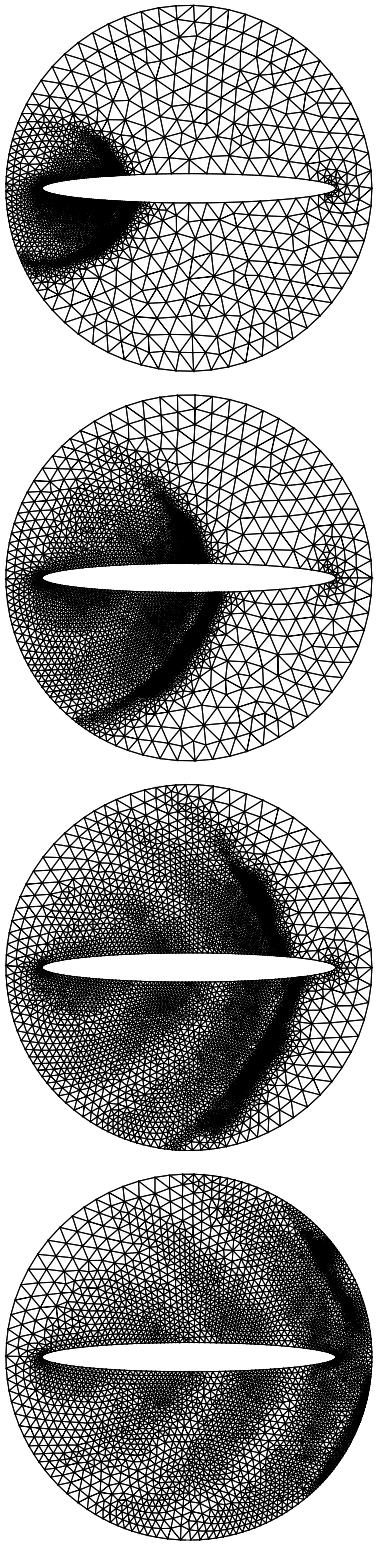

Figure 8. Adaptive mesh for sinusoidal incident plane wave problem at snapshots in time: t=0.5, 1.0, 1.5, 2.0.

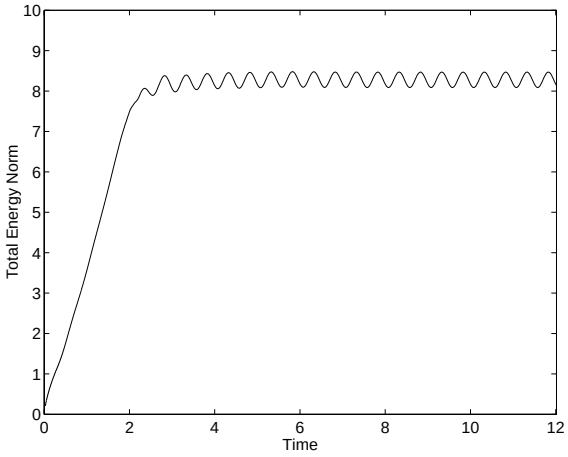

Figure 9. Total energy norm (28) computed within the computational domain Ω.

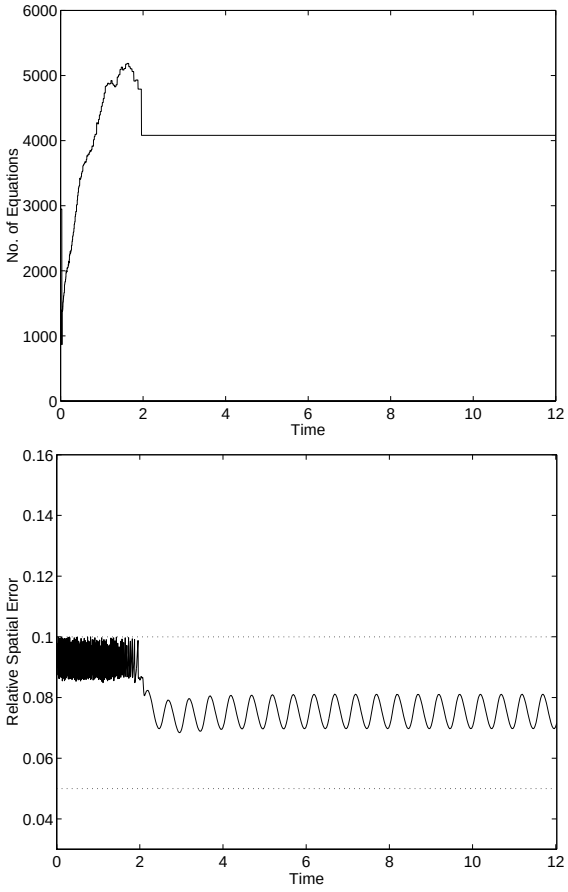

Figure 10. Adaptive mesh based on control parameters: $\eta_s^{TOL} = 10\%$. $(\beta_{s1}, \beta_{s2}) = (0.5, 1.2)$, $K_s = 20$, $h_{max} = 0.12$.

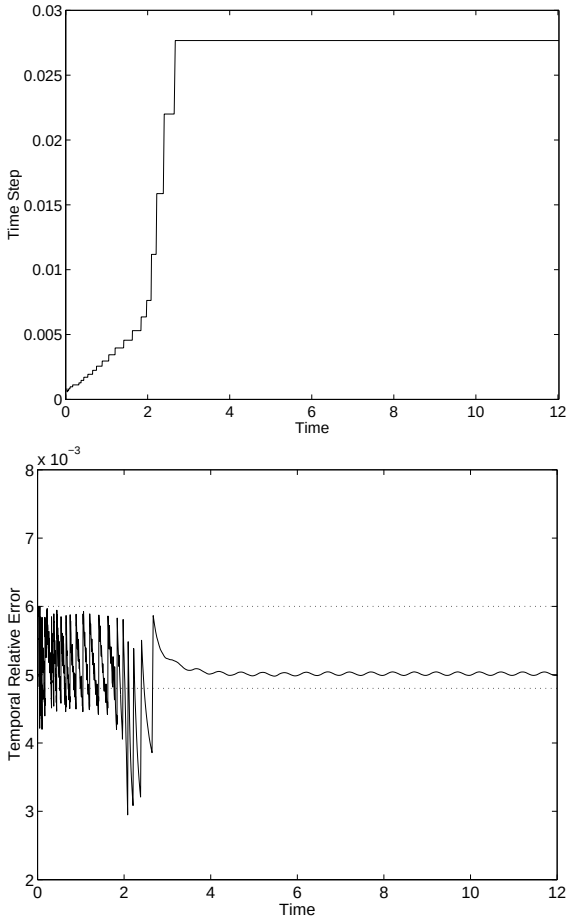

Figure 11. Adaptive time-steps based on control parameters: $\eta_t^{TOL} = 0.6\%$. $(\beta_{t1}, \beta_{t2}) = (0.8, 1.1)$. $K_t = 10$.

In the above, $\beta = \omega_r t - 3\sqrt{6}$ where ω_r is the dominant frequency of the excitation. A Ricker pulse wavelet is chosen for its well defined and controllable frequency band, see [14].

We use our adaptive DGFEM with high-order accurate radiation boundary conditions to track the scattered field as the Ricker pulse reflects from the rigid ellipse.

Fig. 12 shows the adaptive DGFEM scattered field solution at representative snapshots in time. The contours are rescaled at each time step, so that the max/min values at a given time step are distributed evenly between thirty contour lines. Fig. 13 shows the corresponding mesh efficiently tracking the scattered field as the wave pulse moves through the computational domain. A fine mesh is distributed in regions of high gradient while a coarse mesh is distributed in quiescent regions. Initially, the scattered field is localized near to the surface of the scatterer and then expands as the plane-wave pulse progresses past the elliptic scatterer. The incident wave leaves the computational domain just after

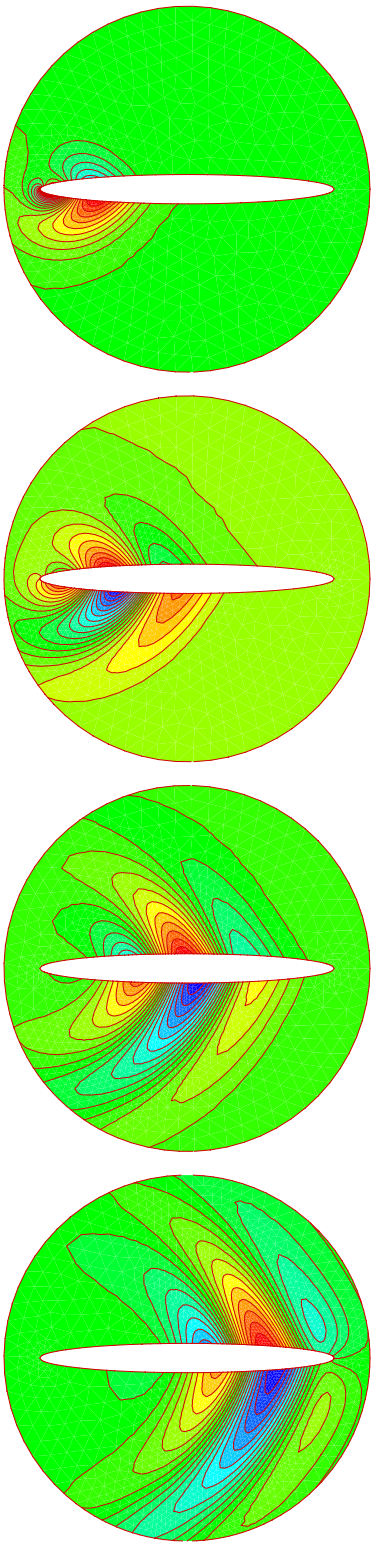

Figure 12. Scattered field solution from Ricker pulse at snapshots in time: $t = (1.0, 2.5),\ \delta t = 0.5$

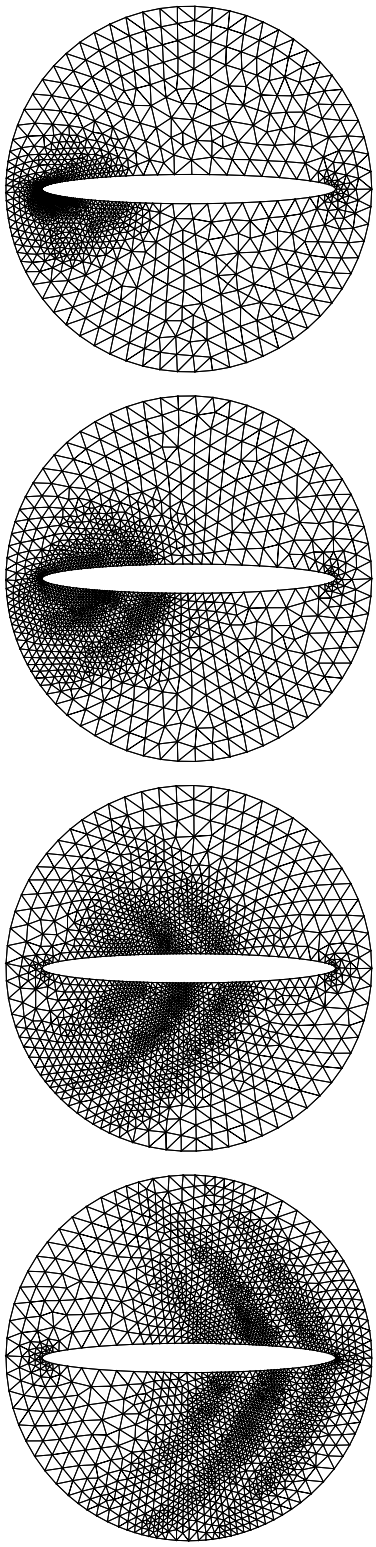

Figure 13. Adaptive mesh tracking Ricker pulse scattered solution.

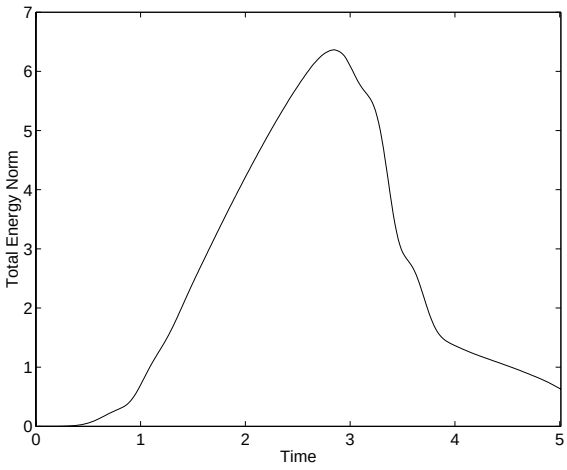

Figure 14. Total energy norm (28) computed within the computational domain Ω.

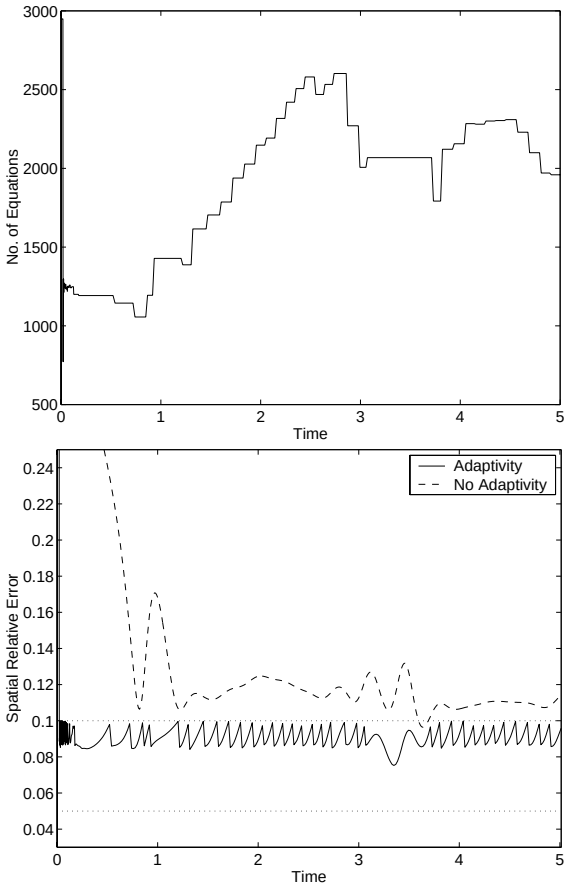

Figure 15. Adaptive mesh controlled by: $\eta_s^{TOL} = 10\%$. $(\beta_{s1}, \beta_{s2}) = (0.5, 1.1)$, $K_s = 20$, $h_{max} = 0.12$.

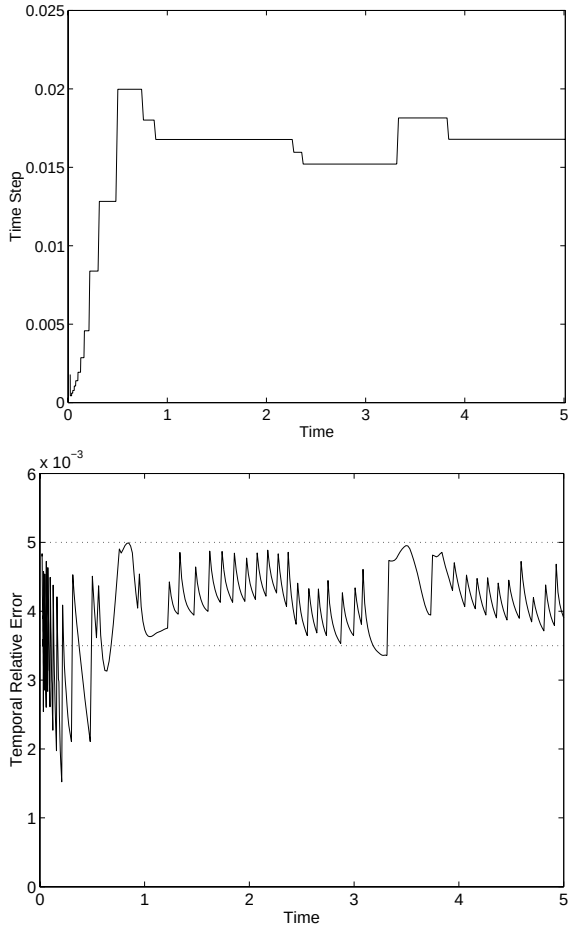

Figure 16. Adaptive time-steps controlled by: $\eta_t^{TOL} = 0.5\%$, $(\beta_{t1}, \beta_{t2}) = (0.7, 1.2)$. $K_t = 10$.

$t = 3.5$. The backscatter continues with significant amplitude up to $t = 5$.

The global energy norm defined in (26),(28) is computed and monitored as the solution progresses. As shown in Fig. 14, initially the energy of the scattered field builds-up within the computational domain as the incident wave pulse progresses. After some time, the scattered field waves are transmitted through the circular truncation boundary Γ, giving rise to radiation damping.

Fig. 15 shows the total degrees-of-freedom (DOF) count as the solution progresses in time. The number of DOF adapt to maintain a maximum spatial error of $\eta_s \leq 10\%$. The results also show that if the initial uniform mesh of 2989 nodes is fixed for all time, the spatial error is significantly higher than the 10% target and requires many more DOF compared to the adaptive solution. The adaptive time-step size is shown in Fig. 16. Initially the time steps are small and then gradually increase to maintain a

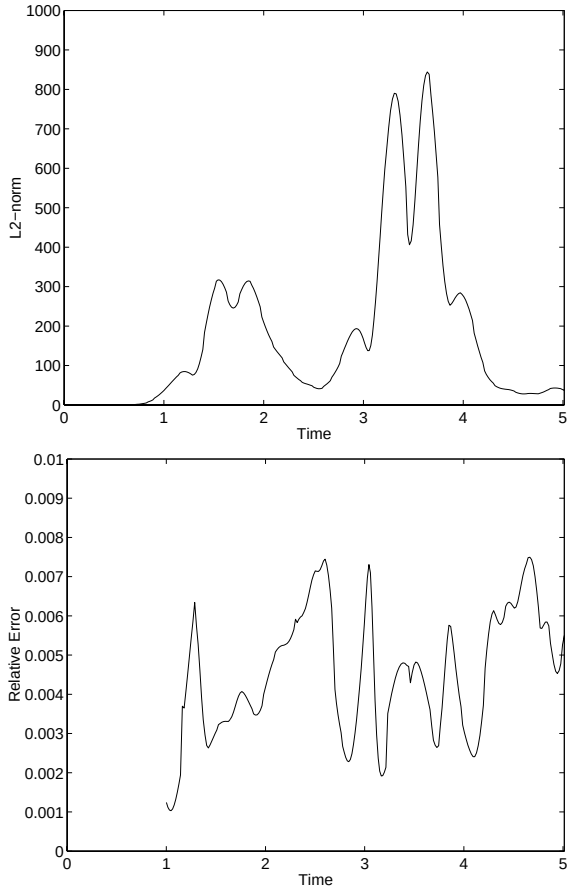

Figure 17. Error estimate for radiation boundary equations. (Top) L_2-norm $||\boldsymbol{w}||_n$, defined in (31). (Bottom) Relative error η_w, as measured from temporal jump conditions.

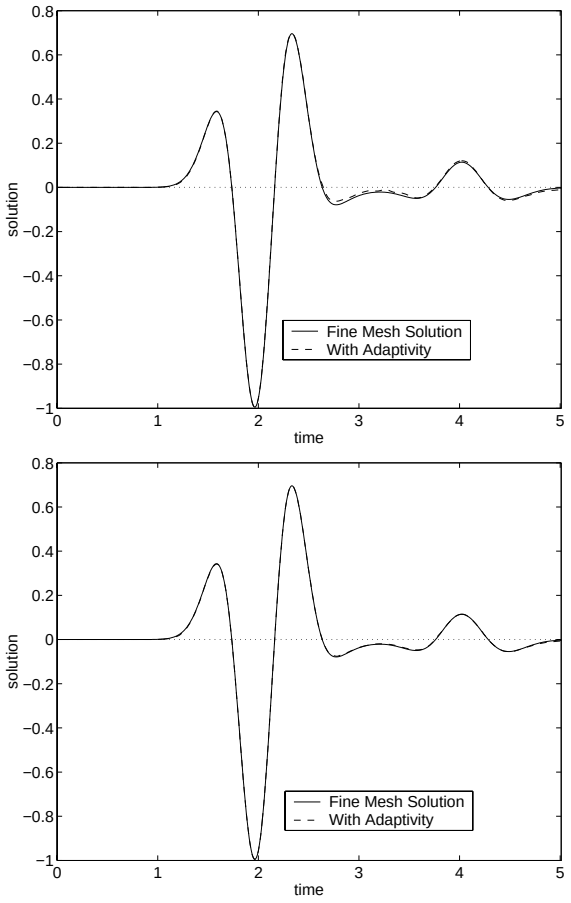

Figure 18. Adaptive solution compared with a fine mesh solution at observation point 1: $(0, -b)$; (Top) $\eta_s^{TOL} = 10\%$. (Bottom) $\eta_s^{TOL} = 6.5\%$.

target temporal error range, with maximum relative error $\eta_t \leq 0.5\%$.

Fig. 17 shows the norm of the auxiliary boundary functions, $||\boldsymbol{w}||_n$, defined in (31) and relative temporal error η_w defined in (34). The results show that the norm of the boundary functions is approximately zero up until the initial time, $t = 0.8$, at which significant amplitudes of the interior scattered field reaches the circular truncation boundary. For this simulation, the relative error is below the tolerance $\eta_w < 1.0\%$, for all time-steps.

Fig. 18 shows a comparison of the adaptive and fine mesh solution at the bottom surface of the ellipse as illustrated in Fig. 4. The results show that by decreasing the estimated error tolerances, we are able to match the fine mesh solution accurately with significantly fewer nodes and time-steps.

Figure 19 shows that only a few iterations per time-step are needed to advance the solution using our multi-level

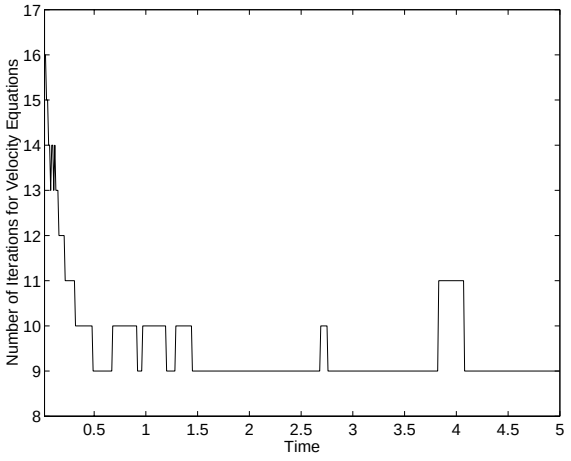

Figure 19. Total number of iterations = 4747 over interval t=(0,5).

iteration algorithm with error tolerance $\varepsilon = 10^{-6}$.

CONCLUSIONS

Comprehensive adaptive procedures with efficient solution algorithms for the time-discontinuous Galerkin space-time finite element method (DGFEM) including high-order accurate nonreflecting boundary conditions for unbounded wave problems are developed. The procedures are implemented in two-dimensions but are also valid for three-dimensional problems as well.

Computationally efficient matrix structures are derived for high-order polynomial interpolation, reducing the size of the equations to be solved in half. The coupled interior/boundary equations are solved efficiently using sparse multi-level iterative algorithms based on the Gauss-Seidel method. Due to the local nature of wave propagation, the iterative strategies require only a few iterations per time step to resolve the solution to high accuracy. Further cost savings are obtained by diagonalizing the mass and boundary damping matrices. In this case the algebraic structure decouples the diagonal block matrices for the velocity equations, giving rise to a very fast, unconditionally stable explicit iterative method. For accurate data transfer (projection) between adaptive meshes, a new superconvergent interpolation (SI) method was developed for low-order 3-node triangle elements. The procedures are easily extended to quadrilaterals and tetrahedra. Numerical studies of transient scattering demonstrate as wave pulses propagate throughout the mesh, elements are refined near wave fronts, and unrefined where the solution is smooth or quiescent. Time-steps are also adjusted to maintain given error tolerances. The result, is a very efficient, accurate and reliable, self-adaptive method.

Further work we are currently pursuing is the implementation of the iterative solution methods presented with quadratic and higher-order polynomials in space and time, within our reduced algebraic matrix structure, and combined with an hp-adaptive strategy in both space and time. Using this approach, it is expected that exponential rates of convergence can be achieved, not only in space, but also in time. We are also developing local space-time elements constructed from sub-time steps within different elements in a space-time slab. The end result, will be a truly local hp-adaptive method which can distribute elements locally in both space and time to efficiently track transient waves from structures subjected to scattering and/or radiation with high-frequency, compact wavelet pulses including explosive shock waves with sharp gradients.

ACKNOWLEDGMENT

Support for this work was provided by the National Science Foundation under Grant CMS-9702082 in conjunction with a Presidential Early Career Award for Scientists and Engineers (PECASE), and is gratefully acknowledged.

REFERENCES

[1] T.J.R. Hughes, Hulbert, G., 1988; 'Space-time finite element methods for elastodynamics: Formulations and error estimates', *Computer Methods in Applied Mechanics and Engineering*, 66, 339-363.

[2] G. Hulbert, 1992; 'Time finite element methods for structural dynamics', *International Journal for Numerical Methods in Engineering*, Vol.33, 307-331.

[3] L.L., Thompson, P.M. Pinsky, 1996; 'A Space-time finite element method for structural acoustics in infinite domains, Part I: Formulation, Stability, and Convergence', *Computer Methods in Applied Mechanics and Engineering*, 132, 195-227.

[4] L.L., Thompson, P.M. Pinsky, 1996; 'A Space-time finite element method for structural acoustics in infinite domains, Part II: Exact time-dependent non-reflecting boundary conditions', *Computer Methods in Applied Mechanics and Engineering*, 132, 229-258.

[5] L.L. Thompson, P.M. Pinsky, 1996; 'A Space-time finite element method for the exterior structural acoustics problem: Time-dependent radiation boundary conditions in two spatial dimensions', *International Journal for Numerical Methods in Engineering*, 39, 1635-1657.

[6] L.L. Thompson, P.M. Pinsky, 1996; 'A space-time finite element method for the exterior acoustics problem', *Journal of the Acoustical Society of America*, 99 (6), 3297-3311.

[7] I. Harari, K. Grosh, T.J.R. Hughes, M. Malhotra, P.M. Pinsky, 1996; J.R. Stewart, L.L. Thompson, 'Recent Developments in Finite Element Methods for Structural Acoustics', *Archives of Computational Methods in Engineering,* 3, 132-311.

[8] L.L. Thompson, 1995; 'A multi-field space-time finite element method for structural acoustics', *Proceedings of the 1995 Design Engineering Technical Conferences*, Boston, Mass., Sept. 17-21, *Acoustics, Vibrations, and Rotating Machines*, Vol. 3, Part B, ASME, pp. 49 - 64.

[9] X.D. Li, N-E Wiberg, 1998; 'Implementation and adaptivity of a space-time finite element method for structural dynamics', *Computer Methods in Applied Mechanics and Engineering*, 156, 211-229.

[10] N-E Wiberg, X.D. Li, 1999; 'Adaptive finite element procedures for linear and non-linear dynamics', *International Journal for Numerical Methods in Engineer-*

ing, 46, 1781-1802.

[11] R. Huan, L.L. Thompson, 2000; 'Accurate Radiation Boundary Conditions for the Time-Dependent Wave Equation on Unbounded Domains', *International Journal for Numerical Methods in Engineering*, 47, 1569 - 1603.

[12] L.L. Thompson, R. Huan, D. He, 2001; 'Accurate radiation boundary conditions for the two-dimensional wave equation on unbounded domains', *Computer Methods in Applied Mechanics and Engineering*, 191 , 311-351.

[13] L.L. Thompson, R. Huan, 2000; 'Implementation of Exact Non-Reflecting Boundary Conditions in the Finite Element Method for the Time-Dependent Wave Equation', *Computer Methods in Applied Mechanics and Engineering*, 187 , 137-159.

[14] L.L. Thompson, R. Huan, 2000; 'Computation of Far Field Solutions Based on Exact Nonreflecting Boundary Conditions for the Time-Dependent Wave Equation', *Computer Methods in Applied Mechanics and Engineering*, 190, 1551-1577.

[15] L.L. Thompson, R. Huan, 1999; 'Finite Element Formulation of Exact Non-Reflecting Boundary Conditions for the Time-Dependent Wave Equation', *International Journal for Numerical Methods in Engineering*, 45, 1607-1630.

[16] L.L. Thompson, R. Huan, 1999; 'Computation of Transient Radiation in Semi-Infinite Regions Based on Exact Nonreflecting Boundary Conditions and Mixed Time Integration', *Journal of the Acoustical Society of America*, 106 (6), pp. 3095-3108.

[17] O. C. Zienkiewicz, J. Z. Zhu, 1992; 'The superconvergent patch recovery and a posterior error estimates. Part 1: The Recovery technique', *International Journal for Numerical Methods in Engineering*, Vol.33, 1331-1364.

[18] O. C. Zienkiewicz, J. Z. Zhu, 1992; 'The superconvergent patch recovery and a posterior error estimates. Part 2: Error Estimates and Adaptivity', *International Journal for Numerical Methods in Engineering*, Vol.33, 1365-1382.

[19] P. Coorevits, P. Ladeveze, J.P. Pelle, 1995; 'An automatic procedure with a control of accuracy for finite element analysis in 2D elasticity', *Computer Methods in Applied Mechanics and Engineering*, 121, 91-120

[20] A. Bayliss, E. Turkel, 1980; 'Radiation boundary conditions for wave-like equations', *Commun. Pure Appl. Math.* 33 , 707-725.